Biomedical Signal Processing and Control 80 (2023) 104312

Contents lists available at ScienceDirect

Biomedical Signal Processing and Control

journal homepage: www.elsevier.com/locate/bspc

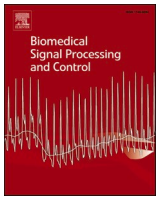

Deep learning-based classification of healthy aging controls, mild cognitive impairment and Alzheimer's disease using fusion of MRI-PET imaging

V.P. Subramanyam Rallabandi, Krishnamoorthy Seetharaman *

Dept. of Computer and Information Sciences, Annamalai University, Annamalai Nagar, Chidambaram, Tamil Nadu, India

ARTICLE INFO

Keywords:
Deep learning
Convolutional neural networks
Magnetic resonance imaging
Positron emission tomography
Dementia
Alzheimer's disease

ABSTRACT

Automated detection of dementia stage using multimodal imaging modalities will be helpful for improving the clinical diagnosis. In this study, we develop the Inception-ResNet wrapper model in differentiating the healthy controls (HC), mild cognitive impairment (MCI), and Alzheimer's disease (AD) using conjoint magnetic resonance imaging (MRI) and positron emission tomography (PET) scans. We use T1-weighted MR and PET images of individuals aged between 42 and 95 years, including HC, MCI and AD patients. We first perform 3D tissue segmentation of MR images after skull striping. The atlas-based segmented MR image tissue is fused with PET image. Then we transform PET images from RGB to HSI color space and apply fusion of MRI with PET images using two-dimensional Fourier and discrete wavelet transform (DWT) and then reconstruct the MR-PET fused image using inverse Fourier and DWT methods. After the fusion of MRI and PET imaging modalities, we used 60 % training, 20 % for validation and the remaining 20 % as a test set using various convolutional neural networks. We found the proposed model as the best classifier with an accuracy of 95.5 %, 94.1 % and 95.9 % in classifying HC vs MCI, MCI vs AD and AD vs HC respectively when compared to the existing methods. We conclude that the proposed deep learning model has potential in automated classification of healthy and dementia stages using combined MRI and PET modalities with good performance.

1. Introduction

Alzheimer's disease (AD) is a progressive disease due to dementia (memory and cognition loss) due to cortical neurodegeneration when compared to healthy aging. Currently the prevalence of AD is about 24 million people worldwide. Early detection of dementia stage will be helpful for efficacious treatment as delayed therapy will not be helpful in arresting the disease progression. Hence early imaging-based diagnosis among the dementia stages are required. Till date, most of the available methods are manual and semi-automated and hence fully automated reliable imaging methods are needed. However, automated methods are more useful without human intervention that could differentiate stages of dementia either correlated with clinical scale or cognitive score.

Various machine learning (ML) methods using structural magnetic resonance imaging (sMRI) have been proposed for classifying various stages of dementia [1–3]. sMRI-based disease atrophy index [4,5], brain asymmetry pattern [6], identification of AD-related brain patterns [7] including disease progression of AD [8]. Several studies have been proposed using fluorodeoxyglucose-positron emission tomography (FDG-PET) and of amyloid deposition using amyloid PET can help in differentiating AD from healthy cognitive individuals (HC). An association between AD and hypometabolism was found in several brain regions, such as the hippocampus [9] and parieto–temporal and posterior cingulate cortices [10]. Similarly, AD subjects compared to HC have shown higher amyloid burden in overall cortex and all cortical regions (precuneus, anterior and posterior cingulate, and frontal median, temporal, parietal and occipital cortex) [11]. Also, the characteristic patterns of cerebral glucose metabolism rate can help in AD classification and prediction of conversion from MCI to AD [12,13]. Anatomical atlas region of interests (ROIs)-based gaussian mixture model and model selection are combined to predict discriminative brain metabolism patterns [14]. The evidence of the association of hypometabolism and amyloid burden with AD encouraged the use of FDG-PET and amyloid PET as a suitable biomarker for AD classification. However, it is reliable for AD but not suitable biomarker for early MCI stage.

Longitudinal studies were also reported for the progression of the disease or stable condition. Some group analysis-based studies have revealed differences in amyloid burden in various brain regions in

* Corresponding author.
E-mail addresses: rvpsubramanyam@gmail.com (V.P. Subramanyam Rallabandi), kseethaddeau@gmail.com (K. Seetharaman).

https://doi.org/10.1016/j.bspc.2022.104312
Received 27 March 2022; Received in revised form 11 September 2022; Accepted 8 October 2022
Available online 25 October 2022
1746-8094/© 2022 Elsevier Ltd. All rights reserved.

different subject groups; higher amyloid burden has been found in progressive mild cognitive impairment (pMCI) than those in stable MCI (sMCI) individuals [15,16]. Another study used the average regional intensity and inter-hemispheric symmetry between the parcellated regions as features for support vector machines (SVM)-based classification [17]. The prominent goal of these methods is to simultaneously select the informative voxels as features and used to investigate the prediction of AD conversion based on FDG-PET images at various time-points [18]. Discriminative voxels of the images were selected based on mutual information criterion, SVM and Gaussian naive bayes were used for classification. The classification based on stage-specific categories of pMCI demonstrated better predictive accuracy than did the overall classification of pMCI and sMCI [19]. Another study used quantification of plaque levels in different regions using the intensity values of all the voxels of ^{18}F-flutemetamol PET scans as features for SVM-based classification of AD versus HC, and pMCI versus sMCI subjects [20]. Feature dimensionality reduction method, non-negative matrix factorization projections to functional brain images was applied and then selected several subsets of these projections, and classified using SVM [21]. Thus, feature selection also plays a role in improving accuracy.

The combination of sMRI features with PET and cerebrospinal fluid (CSF) biomarkers is another dimension. These biomarkers yield complementary information, i.e., different modalities capture disease information from different perspectives, thereby improving understanding of the disease pattern over that presented by one modality. The regional gray matter (GM) volumetric measures, CSF biomarkers, voxel-based FDG-PET intensities, and APOE genotype were trained using random forest for AD and MCI classification [22]. In earlier studies, the combined regional volumetric measures, and regional cerebral blood flow were used for MCI classification using SVM [23]. In addition, the spatial patterns of brain atrophy-AD index with CSF biomarkers were combined to predict conversion from MCI to AD using SVM [24]. Further, FDG-PET and GM density values of all the voxels of selected ROIs and the average of all the voxels of selected ROIs were classified AD using SVM classifier [25]. The combined regional GM volume, regional average PET intensity, and CSF biomarkers as features, and proposed a matrix-similarity-based loss function for better classification using SVM [26]. Similarly, regional thickness measures, regional correlative measures (calculated from thickness measures) and APOE genotype were used to classify AD using SVM classifier, and further prediction of AD conversion [27]. Also, hippocampal volume and CSF biomarkers were classified AD and MCI using the SVM classifier [28].

The combination of sMRI, PET, and CSF biomarkers together with genetic data and neuropsychological status exam scores has also been common. A study was combined with cognitive scores, APOE genotype, and CSF biomarkers to predict conversion from MCI to AD [29]. Similarly, the combined hippocampal, ventricular, and temporal lobe volumes, FDG-PET quantitative values, CSF biomarkers, APOE genotype, age, sex, and body mass index were used SVM-based AD and MCI classification [30]. In addition, the combined average regional cortical thickness, standard deviation of thickness, average regional surface area and cortical volume features from sMRI with CSF biomarkers and neuropsychological status exam scores using SVM classifier [31]. The use of straightforward feature concatenation may be considered desirable but the method suffers from a major drawback as it treats all the features are equivalent, it provides no way to account for the different natures of features extracted from different modalities [32,33]. The fusion strategies may either combine the results of classification rules trained on the individual modalities [34] or use special combination rules to combine features before training [35,36]. The multi-task learning [37], domain transfer learning [38] and semi-supervised multimodal manifold-regularized transfer learning [39] have been proposed for the prediction of MCI conversion. Recently, multi-modal ML classification methods have been reported using ^{18}Fluorine PET, sMRI and fMRI for the classification of AD and MCI [40,41], MCI classification and prediction of progression to AD [42], graph-based transductive learning [43], and joint human connectome project multi-modal parcellation using logistic regression and recursive feature elimination [44]. The recent studies advocated the use of multi-modal imaging.

Various deep learning (DL)-based MRI-PET imaging approaches have been proposed using combination of convolutional and recurrent neural network (CNN-RNN) [45], traditional bidirectional long short-term memory (biLSTM) [46] and fully stacked (FSbiLSTM) [47] including the combination of neuroimaging features with genomics data [48] as well as post-mortem pathological correlation [49]. Most of the current diagnosis utilize single imaging modality and the need for multimodality imaging with the technological advances majorly impact on clinical diagnosis with structural, diffusion, functional MRI (fMRI) [50], diffusion and functional imaging [51]. These recent developments have already had a critical positive effect on the automated clinical diagnosis and prognosis with portent continued quick improvements utilizing ML and DL methods. Here, we propose a DL-based Inception-ResNet50 wrapper model in classifying MCI and AD dementia patients from HC using multi-modal and complementary imaging modalities such as sMRI for better spatial details and combined with functional PET for good temporal resolution. The proposed approach demonstrates an efficient use of the multimodal information provided by the MRI-PET modalities by resolving the current limitations like feature selection biasness as well as feature dimensionality reduction to detect early MCI and AD diagnosis.

2. Methods

2.1. Image acquisition

T1-weighted magnetization prepared rapid gradient-echo (MP-RAGE) images were acquired on a 1.5 T and 3 T Siemens scanner taken from Open Access Series of Imaging Studies (OASIS) online dataset contains about 1098 individuals over 2000 MR sessions, including multiple structural and functional sequences. The MR image acquisition details are repetitive time = 9.7 msec, echo time = 4.0 msec, flip angle = 10^0, inversion time = 20 msec, orientation = sagittal, thickness = 1.25 mm, slice gap = 0 mm, no. of slices = 128 and pixel resolution = 256x256. The subjects include both men and women aged between 42 and 95 years with 605 cognitively healthy controls and 493 demented individuals at different stage and has been clinically and cognitively evaluated using clinical dementia rating (CDR scale:0–3; 0 being cognitively normal, 0.5: MCI, 1: mild AD, 2 moderate AD and 3 being severe AD) and mini-mental state examination (MMSE:1–30 score) to determine dementia stage or cognitively healthy.

Functional imaging using ^{18}F- fluorodeoxyglucose (FDG) was performed on the high resolution (HR) PET scanner with 1500 raw imaging scans. The plasma glucose concentration was measured prior to tracer administration and individuals blood glucose concentrations >=165 were excluded from the study. Participants received an I.V. bolus injection of 5 mCi of 18F-FDG followed by a dynamic 60 min (consisting of 24 × 5 *sec* frames, 9 × 20 *sec* frames, 10 × 1 min frames and 9 × 5 min frames) PET acquisition.

2.2. Preprocessing

The PET images are in red, green and blue (RGB) color space transformed based on HSI (hue, saturation, intensity) space and applied Fourier transform (FT) on both MRI and PET images. Since the HSI space has the ability to separate the intensity of the intrinsic color information, and they are affected by lighting changes, characteristic of the images. Further, low-pass and high-pass spatial filtering was done using discrete wavelet transform (DWT). The fusion of both low and high pass filters on MRI and PET was done using inverse DWT and finally retransformed to HSI color space. The MRI-PET fusion workflow process is given in Fig. 1. The conversion of RGB to HSI color space for PET image was transformed using the below expressions. Initial RGB image is normalized in

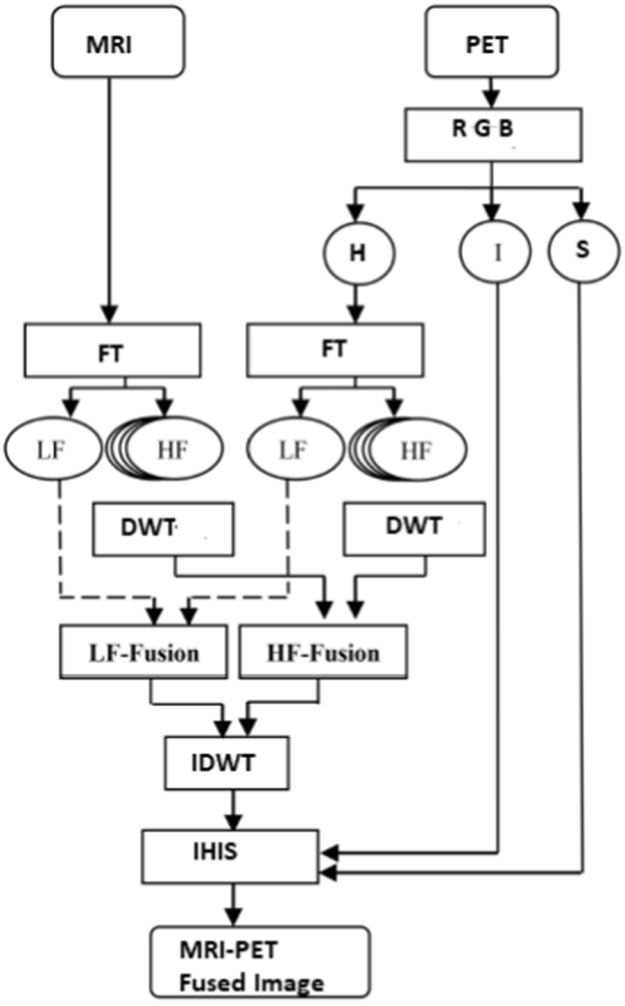

Fig. 1. MRI-PET fusion workflow: MRI images were applied Fourier transform and PET images were transformed from RGB color space to HIS color space and then performed DWT fusion by decomposing into low-pass and high-pass filters and performed inverse DWT to reconstruct MRI-PET fusion image.

the range [0, 1] and estimated the HSI components [53].

$$\theta = \cos^{-1}\left(\frac{\frac{1}{2}[(R-G)+(R-B)]}{\left[(R-G)^2+(R-B)(G-B)^{1/2}\right]}\right) \tag{1}$$

$$Hue(H) = \theta \ if \ B \le G \ else (360-\theta) \tag{2}$$

$$Saturation(S) = 1 - \frac{3}{R+G+B}[\min(R,G,B)] \tag{3}$$

$$Intensity(I) = \frac{1}{3}(R+G+B) \tag{4}$$

The raw MRI slice represented using two-dimensional (2D) Fourier transform is given by [54].

$$F(k,l) = \sum_{i=0}^{N-1}\sum_{j=0}^{N-1} f(i,j)e^{-i2\pi\left(\frac{ki}{N}+\frac{lj}{N}\right)} \tag{5}$$

where *f(i,j)* is the image in the spatial domain and the exponential term is the basis function corresponding to each point *F(k,l)* in the Fourier space which can be interpreted as the value of each point *F(k,l)* is obtained by multiplying the spatial image with the corresponding base function and summing the result. The basis functions are sine and cosine waves with increasing frequencies, i.e. *F(0,0)* represents the DC-component of the image which corresponds to the average brightness and *F(N-1,N-1)* represents the highest frequency.

In a similar way, the Fourier image can be re-transformed to the spatial domain. The inverse Fourier transform is given by.

$$f(a,b) = \frac{1}{N^2}\sum_{k=0}^{N-1}\sum_{l=0}^{N-1} F(k,l)e^{i2\pi\left(\frac{ka}{N}+\frac{lb}{N}\right)} \tag{6}$$

in which $\frac{1}{N^2}$ is the normalization term in inverse transformation. This normalization is sometimes applied to the forward transform instead of the inverse transform, but should not be used for both.

To obtain the result for the above equations (5 and 6), a double sum has to be calculated for each image point. However, the Fourier Transform is separable and can be written as.

$$F(k,l) = \frac{1}{N}\sum_{b=0}^{N-1} P(k,b)e^{-i2\pi\left(\frac{lb}{N}\right)} \tag{7}$$

$$\text{where } P(k,b) = \frac{1}{N}\sum_{a=0}^{N-1} f(a,b)e^{-i2\pi\left(\frac{ka}{N}\right)} \tag{8}$$

Using these two formulas, the spatial domain image is first transformed into an intermediate image using N one-dimensional Fourier Transforms. This intermediate image is then transformed into the final image, again using N one-dimensional Fourier Transforms. Expressing the 2D Fourier Transform in terms of a series of 2 N one-dimensional transforms decreases the number of required computations by employing Fast Fourier Transform (FFT). Since FT is not localized in time and space, MRI images were further applied 2D discrete wavelet transform (DWT) of image I is calculated by passing it through a series of filters. First the samples are passed through a low-pass filter with impulse response g resulting in a convolution operator (*) of the two which is given by.

$$y[n] = (I^*g)[n] = \sum_{j=0}^{N-1}\sum_{k=0}^{N-1} I(j,k)g[n-j]^*g[n-k] \tag{9}$$

The image is also decomposed simultaneously using a high-pass filter, *h*. The outputs give the detail coefficients (from the high-pass filter) and approximation coefficients (from the low-pass). However, the two filters are related to each other and half the frequencies are removed as per Nyquist's rule as follows:

$$y_{low}[n] = (I^*g)[n] = \sum_{j=0}^{N-1}\sum_{k=0}^{N-1} I(j,k)g[2n-j]^*g[2n-k] \tag{10}$$

$$y_{high}[n] = (I^*h)[n] = \sum_{j=0}^{N-1}\sum_{k=0}^{N-1} I(j,k)h[2n-j]^*h[2n-k] \tag{11}$$

The filter output of the low-pass filter, *g* is then subsampled by 2 and further processed by passing it again through a new low-pass filter *g* (approximation coefficients) and a high-pass filter, *h* (detail coefficients) with half the cut-off frequency of the previous one [55]. This decomposition is repeated to further increase the frequency resolution and the approximation coefficients decomposed with high and low-pass filters and then down-sampled. After one level of transform, we obtain N/2 coefficients by splitting into even and odd indexed positions in the lifting scheme (LS). This process is recursively repeated which can be shown as a cascading and filter banks representing a sub-space with a different time–frequency localization. We used PyWavelets package [56]. Instead of traditional LS (left-hand, right-hand and inner columns), we implemented the horizontal filtering (lower and upper boundaries and inner rows) DWT kernel and then followed by vertical DWT. Then estimate the thresholds for all the detailed coefficients using soft thresholding method in which by setting to zero coefficients whose absolute values are lower than applied threshold and shrinking the nonzero coefficients toward zero. Now estimate thresholds for all detail coefficients on all

levels and obtain these matrices for all the detail components and use inverse DWT to reconstruct fusion image.

2.3. MRI-PET registration

MR images of all the subjects were initially bias corrected via N4 and then performed skull stripping. Next perform the atlas-based segmentation of brain tissue on the skull stripped image using Advanced Normalization Tools (ANT) [57] and brain regions defined in Table 1. PET images were smoothed to achieve a common spatial resolution of 8 mm to minimize inter-scanner differences and inter-frame motion correction for the dynamic PET images. We have performed registration in different levels such as individual space and template space. PET/MRI T1 image registration was performed based on the local rigid-body 3D affine transformation; T1-weighted MRI image using rigid-body registration and deformable cubic B-spline interpolation and finally warpped PET with MRI. A rigid-body affine transformation with 12 degrees of freedom (each 3 parameters for translation, rotation, shearing, scaling) used for global registration T_G as follows:

$$T_G(x,y,z) = \begin{pmatrix} \theta_{11} & \theta_{12} & \theta_{13} \\ \theta_{21} & \theta_{22} & \theta_{23} \\ \theta_{31} & \theta_{32} & \theta_{33} \end{pmatrix} \begin{pmatrix} x \\ y \\ z \end{pmatrix} + \begin{pmatrix} \theta_{14} \\ \theta_{24} \\ \theta_{34} \end{pmatrix} \tag{12}$$

For the reference image, I_R and static image, I_S then local registration mapping to a point u, deformation coefficient, h and transformation function, $\widehat{\omega}$ minimize image divergence, K given by.

Table 1
Gyri and Sulci brain region used in segmentation.

Gyri Regions	Sulci Regions
Temporal lobe medial aspect	Anterior ascending ramus of the lateral sulcus
Entorhinal cortex	Anterior horizontal ramus of the lateral sulcus
Parahippocampal gyrus	Anterior occipital sulcus
Fusiform gyrus	Callosal sulcus
Temporal lobe (lateral)	Calcarine sulcus
Superior temporal gyrus	Cingulate sulcus
Middle temporal gyrus	Collateral sulcus
Inferior temporal gyrus	Circular insular sulcus
Transverse temporal gyrus	Central sulcus
Frontal lobe	Caudal superior temporal sulcus, first segment
Superior frontal	Caudal superior temporal sulcus, second segment
Middle frontal gyrus	Caudal superior temporal sulcus, third segment
Rostral	Frontomarginal sulcus
Caudal	First transverse temporal sulcus
Inferior frontal gyrus	Heschl's sulcus
Pars opercularis	Inferior frontal sulcus
Pars triangularis	Interhemispheric sulcus
Pars orbitalis	Intraparietal sulcus
Orbitofrontal gyrus	Inferior temporal sulcus
Lateral division	Lateral H-shaped orbital sulcus
Medial division	Lateral occipital sulcus
Frontal pole	Lateral sulcus
Precentral gyrus	Medial H-shaped orbital sulcus
Paracentral lobule	Olfactory sulcus
Parietal lobe	Occipitotemporal sulcus
Postcentral gyrus	Posterior ascending ramus of the lateral sulcus
Supramarginal gyrus	Paracentral sulcus
Superior parietal lobule	Posterior horizontal ramus of the lateral sulcus
Inferior parietal lobule	Primary intermediate sulcus
Precuneus	Postcentral sulcus
Occipital lobe	Parietooccipital sulcus
Lingual gyrus	Precentral sulcus
Pericalcarine cortex	Pretriangular sulcus
Cuneus cortex	Rhinal sulcus
Lateral occipital cortex	Subparietal sulcus
Cingulate cortex	Superior frontal sulcus (sfrs)
Rostral anterior	Superior rostral sulcus
Caudal anterior	Superior temporal sulcus
Posterior	Temporal incisure
Isthmus	Transverse occipital sulcus

$$\widehat{\omega} = argminK(I_R, I_S{*}h(u/\omega)) \tag{13}$$

Now kernel-based cubic B-spline interpolation [58] was used to evaluate the deformations for a set of control points, ∂_b being set of deformation function and the deformation for any control point, ϑ in the test image is interpolated as given below.

$$C(u/\vartheta) = \sum_b \partial_b \gamma^3\left(\frac{u-\tau b}{\Delta\delta}\right) \tag{14}$$

Now the deformation function, $C(u/\vartheta)$ coefficient is applied on test image i.e.,$h(u/\omega) = C(u/\vartheta)$

where $\gamma^3(u) = \gamma^3(i)\gamma^3(j)\gamma^3(k)$ *and* $u = [i,j,k]^l$ i, j and k are spatial positions of l^{th} slice of I_R and transformed function is given as $\omega = \partial_b$.

Structural T1-weighted image was co-registered with Montreal Neurological Institute (MNI152) T1 brain template. Further, PET to MR registration was performed using a voxel-based algorithm (VBA) that computes image transformations based on the alignment of intensity gradients. Since there is no gold standard score for PET/MRI fusion, we measured using mutual information [59]. A gradient-descent algorithm was used to optimize the normalized mutual information (NMI), a measure of information one random variable contains the other, here image intensity is random variable which is given by.

$$NMI = \frac{H(X)+H(Y)}{H(X,Y)} \tag{15}$$

where *H(X)* and *H(Y)* are the marginal entropies of *X* and *Y* and *H(X,Y)* represents joint entropy. The NMI results between 0 (completely non-aligned images) and 1 (maximum for completely aligned images). The step-wise implementation of the proposed work is given in Fig. 2.

2.4. Deep learning using convolutional neural networks

Various DL models using convolutional neural networks (CNNs) have been proposed such as VGG-16 [60], DenseNet [61], AlexNet [62], ResNet-50 [63], Xception [64] and Inception-V3 [65]. The detailed CNN architecture of the proposed Inception-ResNet wrapper model is shown in Fig. 3. The model used input image size 299x299x3 with maximum pooling size of 3x3 stem model and consequently converting them into different blocks Inception-ResNet A, B, C including two reduction-A and reduction-B blocks. We implemented all the models using Keras and Tensorflow packages in Python 3. Hyperparameter optimization will be helpful in learning and fine tuning the model by varying different parameters such as learning rate = [0.01, 0.001, 0.0001], optimizers = [Adam, root mean square propagation (RMSprop), stochastic gradient descent (SGD)], activation function = [Linear, Rectified linear unit (ReLU), Sigmoid, SoftMax] and epochs = [0 to 50] with step size = 10. The best parameters for the Inception-ResNet wrapper model were found as the learning rate = 0.0001, optimizer = Adam and average pooling with dropout = 0.2 using SoftMax activation function. The images in the entire dataset were split into 60 % training, 20 % validation and the remaining 20 % as test set. We then measured the accuracy, model loss, specificity, sensitivity and area under the curve (AUC) with all the hyperparameters and chose the best model to predict on the test images.

3. Results

Various image-based CNN models were implemented and compared them with the proposed Inception-ResNet50 wrapper model using the fusion of MRI-PET feature maps. ResNet-50 model architecture uses input image size 224x224x3 with 7x7 convolution, maximum pooling size of 3x3 and implemented using three optimizers Adam, RMSprop and SGD by varying number of epochs from 0 to 50 with step size of 10 and with different activation functions. ResNet50 showed accuracy of

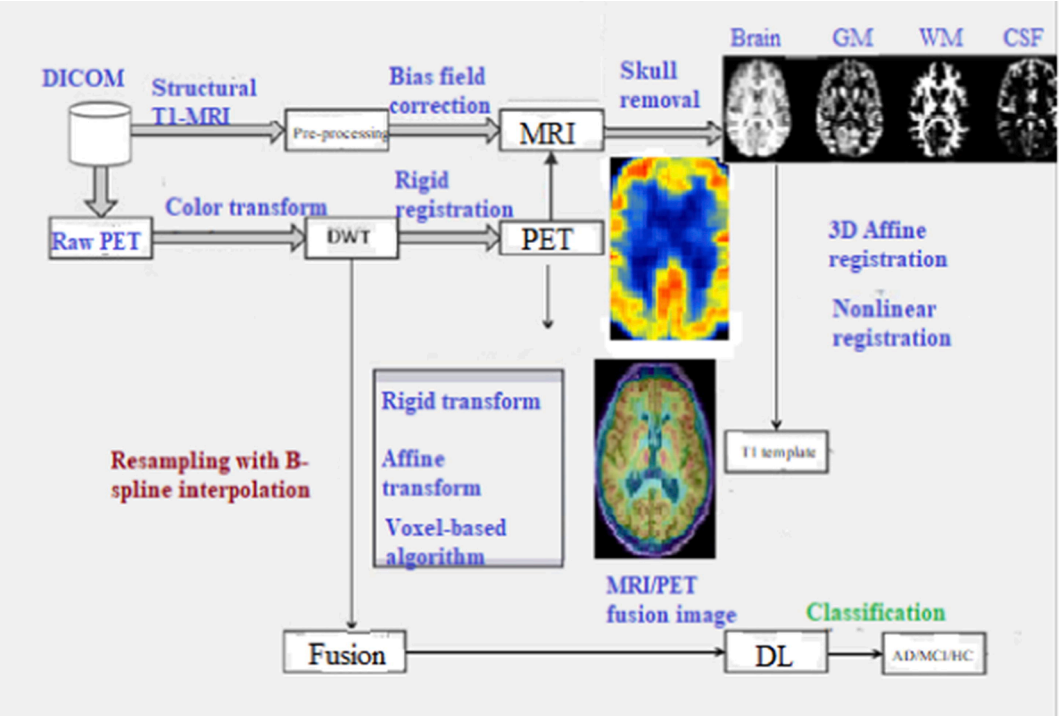

Fig. 2. (a) Schema of the proposed approach: MRI-PET feature fusion; Raw MRI images were preprocessed for bias field correction and perform skull stripping to extract brain tissue and segmentation into gray matter (GM), white matter (WM) and cerebrospinal fluid (CSF); PET images were transformed as shown in Fig. 1 and performed nonlinear affine registration of MRI and PET image to derive MRI-PET fusion image; Deep learning model using Inception and ResNet framework for the classification of HC, MCI and AD individuals.

81.9, 78.5 and 87.9 % for HC vs MCI, MCI vs AD and HC vs AD respectively using Adam optimizer, learning rate = 0.0001 and ReLU activation function. VGG-16 CNN model architecture uses input image size 224x224x3 with 13 convolutional and 3 fully connected layers, maximum pooling size of 2x2 and implemented using three optimizers Adam, RMSprop and SGD by varying number of epochs from 0 to 50 with step size of 10 and with different activation functions. VGG-16 showed accuracy of 82.5, 83.9, 89.4 % for HC vs MCI, MCI vs AD and HC vs AD respectively using Adam optimizer, learning rate = 0.0001 and ReLU activation function. The AlexNet CNN model uses input image size 224x224x3 with 5 convolutional and 3 fully connected layers, maximum pooling size of 3x3 and implemented using three optimizers Adam, RMSprop and SGD by varying number of epochs from 0 to 50 with step size of 10 and with different activation functions. AlexNet showed accuracy of 82.9, 80.5 and 87.9 % for HC vs MCI, MCI vs AD and HC vs AD respectively using Adam optimizer, learning rate = 0.0001 and ReLU activation function. The Inception-V3 CNN model uses 22-layer architecture with parallel blocks of convolutions with different filters, followed by concatenation, captures different features at 1×1, 3×3 and 5×5 and finally clusters them into groups of units based on high correlations. Inception-V3 achieved accuracy of 85.4, 86.7 and 89.1 % for HC vs MCI, MCI vs AD and HC vs AD respectively using Adam optimizer, learning rate = 0.0001 and ReLU activation function. The Xception CNN model uses input image size 299x299x3 with maximum pooling size of 3x3 by capturing cross feature map correlations at 1x1 convolutions and subsequently capture spatial correlations within each channel via 3x3 and 5x5 convolutions. Xception model achieved accuracy of 82.9, 81.5 and 84.9 % for HC vs MCI, MCI vs AD and HC vs AD respectively using Adam optimizer, learning rate = 0.0001 and ReLU activation function. Furthermore, we implemented the Inception-ResNet50 wrapper model with input image size 299x299x3 with maximum pooling size of 3x3, three inception blocks converted into two residual inception blocks as shown in Fig. 3. The proposed Inception-ResNet50 wrapper model achieved the highest classification accuracies of 95.5 %, 94.6 % and 95.7 % for HC vs MCI, AD vs MCI and HC vs AD respectively using Adam optimizer, learning rate = 0.0001 and ReLU activation function as shown in Fig. 4. We noticed that the Inception-ResNet model outperformed the other CNN models. The comparison of all the six CNN models with their performance measures such as accuracy, (the ratio of total correct predictions to sum of all samples), precision, sensitivity or recall (true positive rate) and specificity (true negative rate) were calculated using below formulae:

$$Precision = \frac{TP}{(FP + TP)} \tag{16}$$

$$Recall(orSensitivity) = \frac{TP}{(TP + FN)} \tag{17}$$

$$Specificity = \frac{TN}{FP + TN} \tag{18}$$

$$Accuracy = \frac{(TP + TN)}{(TP + TN + FP + FN)} \tag{19}$$

$$Error = \frac{(FP + FN)}{(TP + TN + FP + FN)} \tag{20}$$

where TP, TN, FP and FN are true positives, true negatives, false positives and false negatives respectively. TP = 192, FP = 8, FN = 7 and TN = 110 in classifying HC and MCI individuals, TP = 111, FP = 6, FN = 3 and TN = 35 in classifying MCI and AD patients, TP = 194, FP = 6, FN = 3 and TN = 35 in classifying HC and AD patients. The comparison of six different CNN models with their performance measures were given in Table 2. The comparison of various DL models using combined MRI and PET modalities were given in Table 3 and the proposed Inception-ResNet model outperformed the existing methods with an accuracy, sensitivity, specificity, ROC of 95, 97.4, 92.76 and 98.5 % respectively. Fig. 5 shows the receiver operating characteristic (ROC) curve which illustrates the

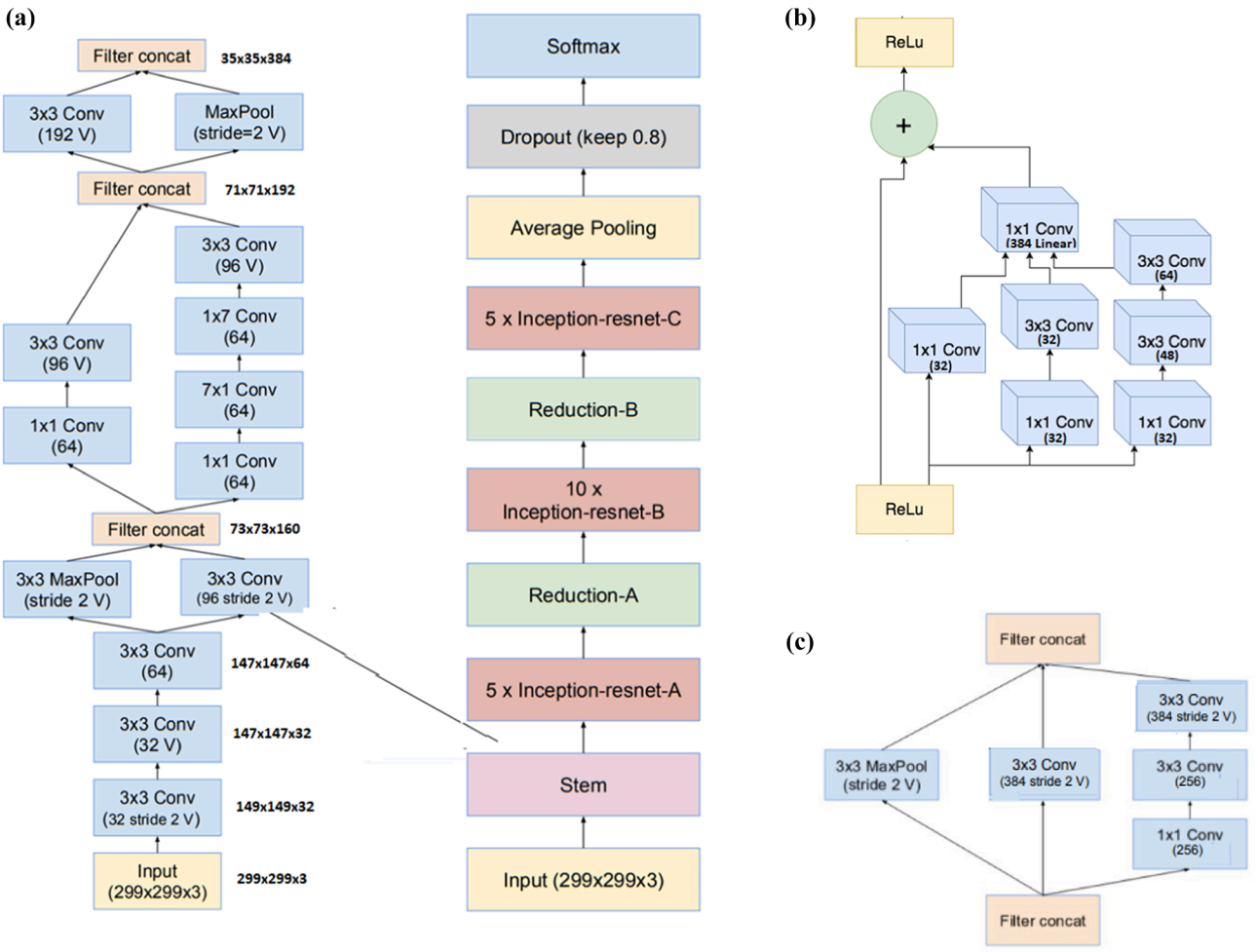

Fig. 3. CNN architecture for the proposed (a) Inception and ResNet50 wrapper model is split into different blocks: (b) Inception-ResNet-A, (c) Reduction-A, (d) Inception-ResNet-B (e) Reduction-B, (f) Inception-ResNet-C with ReLU activation function and average pooling with dropout = 0.2 and finally applied SoftMax activation function to get final output.

trade-off between the false positive rate (on x-axis) and true positive rate (on y-axis) with an AUC of 0.988, 0.981 and 0.989 for HC vs MCI, MCI vs AD and HC vs AD respectively.

4. Discussion

The proposed method was outperformed with the existing CNN models using the combination of MRI and PET imaging modalities. The combination of CNN-RNN model showed an overall accuracy, sensitivity and specificity of 93.3, 92.5 and 93.9 % respectively [45]. Traditional biLSTM model showed an accuracy, specificity and sensitivity of 94.3, 96.6 and 92.4 % respectively [46]. Recently, 3D-CNN FSBiLSTM model showed average accuracies of 94.82, 86.36, and 65.35 % for differentiating AD from HC, progressive MCI from HC, and stable MCI from HC [47]. Various approaches have been proposed in classifying AD, MCI and HC using CNN such as hybrid enhanced independent component analysis-based segmentation of GM on T2-weighted MRI [66], single slice MRI [67] and texture features from MRI image [68]. The multimodal imaging approaches are proposed using sparse hierarchical extreme learning [69], MRI and PET studies [70]; multimodal fusion with DL techniques [71–73]. Also, DL-based fMRI studies have been proposed for early AD and MCI diagnosis [74], static and dynamic functional brain networks [75], spatiotemporal modeling and brain network hub detection [76,77].

Our proposed approach using PET/MRI showed improved performance with respect to the recent ML and DL approaches that are currently available. A recent study based on kurtosis and diffusion features using balanced random forest classifier in classifying MCI, AD and HC [78]. Another MRI study using gray matter density from GM tissue combined with the local gyrification index from WM tissue features for dementia diagnosis of HC, MCI and AD [79]. Several feature selection methods were proposed using local feature selection using SVM classifier [80], and two-stage local feature fusion [81]. Recently, neuroanatomical heterogeneity in normal controls and disease subtypes using semi-supervised DL method has been proposed using Smile-GAN (SeMI-supervised cLustEring-Generative Adversarial Network) [82]. Another study proposed random forest feature selection and deep neural network classification strategy using fuzzy logic learning on a mixed cohort including healthy and AD individuals [83]. A CNN model based on hippocampus achieved a dice similarity coefficient of 0.87 for hippocampal segmentation and also achieved an accuracy of 88.9 % and an AUC of 0.925 for classifying AD vs HC subjects, and an accuracy of 76.2 % and AUC of 0.775 for classifying MCI vs HC subjects [84]. A classifier based on multiple cluster dense convolutional neural networks showed an accuracy of 89.5 .% and an AUC of 0.924 for AD vs HC classification, and an accuracy of 73.8 % and an AUC of 0.775 for classification of MCI vs HC [85]. A CNN-based approach based on cortical volume, surface area and cortical thickness features achieved an accuracy of 79.9 % and an AUC of 0.861 in leave-one-out cross validations [86]. A 3D CNN approach showed accuracy, sensitivity and specificity of 98.90 %, 98.90

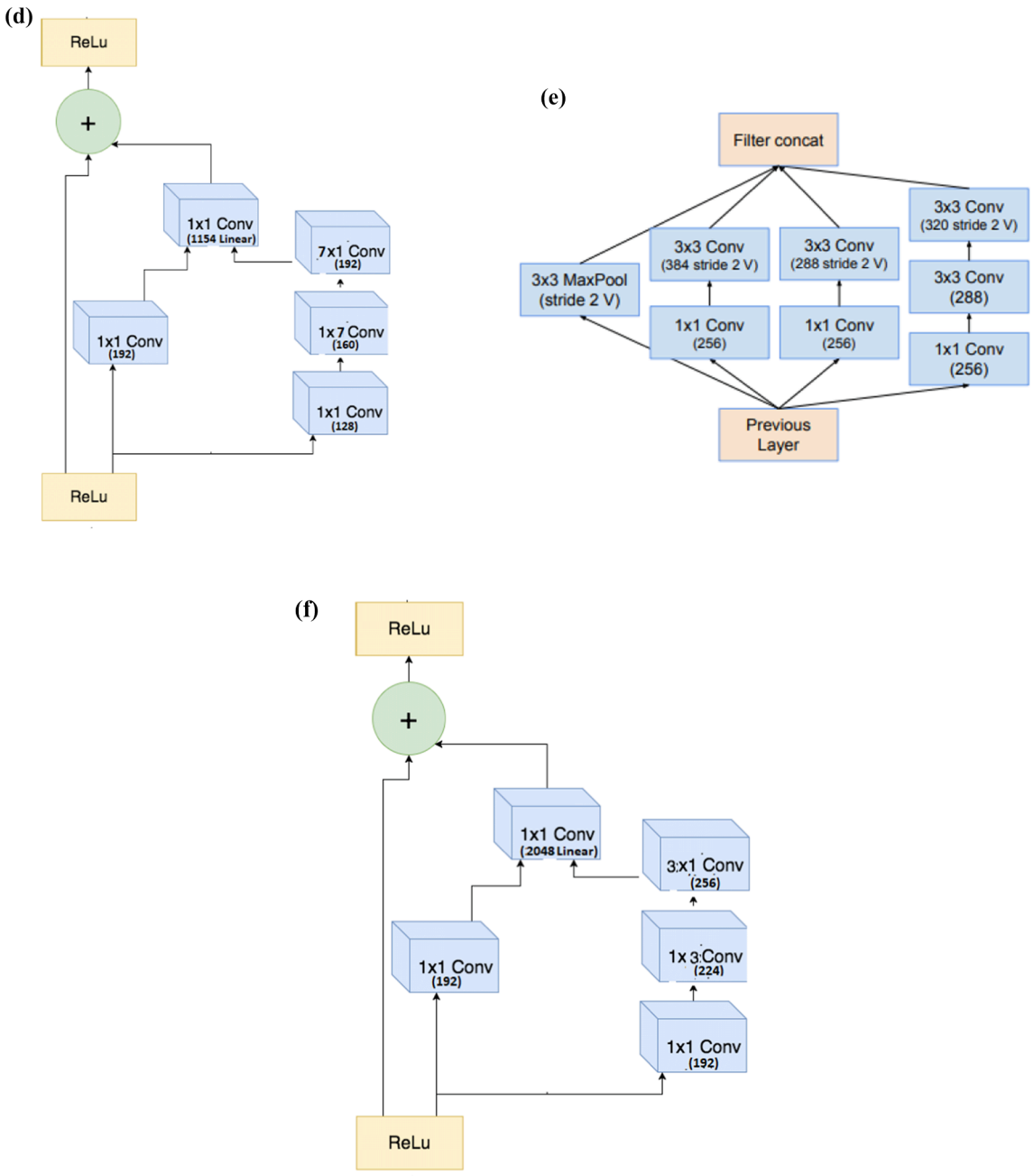

Fig. 3. (*continued*).

% and 98.80 % respectively in classifying HC vs MCI; 99.10 %, 99.80 % and 98.40 % respectively in classifying HC vs AD; 89.40 %, 86.70 % and 84.00 % respectively in classifying MCI vs AD patients [87].

A multi-modal MRI-PET study using a cascaded CNN approach achieved an accuracy of 93.26 % for classification of AD vs HC and 82.95 % for classification MCI converters vs HC [88]. A recent study using the DenseNet-121 based approach achieved overall accuracy of about 90 % in classifying HC, MCI and AD patients [89]. A multi-modal OASIS dataset study classified with an accuracy of 87.0 % using random forest [90]. The cortical thickness-based non-linear SVM approach showed accuracy, sensitivity and specificity of 75.0 %, 75.0 % and 77.0 % respectively in classifying HC,early MCI, late MCI and AD patients [91].

The main advantages of the proposed method over existing methods were firstly, low feature dimensionality derived on fusion image compared to individual imaging modalities. For instance, where one modality has many more features than another (or has variation on a much larger scale), classification algorithms trained on concatenated features may produce prediction models that effectively ignore the other modalities. Secondly, to minimize the misregistration error of MRI-PET, the normalized mutual information was used for the affine global registration and in case of the local registration, non-rigid deformation with cubic B-spline interpolation was used. Thirdly, most biomedical imaging studies do not report handling of imbalanced samples in each group and in this study, we performed data augmentation techniques using random combinations of intensity variation, rotation, translation, horizontal and vertical flipping methods to avoid model overfitting or under fitting. Lastly, the proposed method can handle color PET images without converting to grayscale. However, there are few limitations in our study. Firstly, the prediction of disease progression or stable (non-converters) over time (longitudinal data). Also, another limitation of multimodal imaging is collection of data on same individuals which is

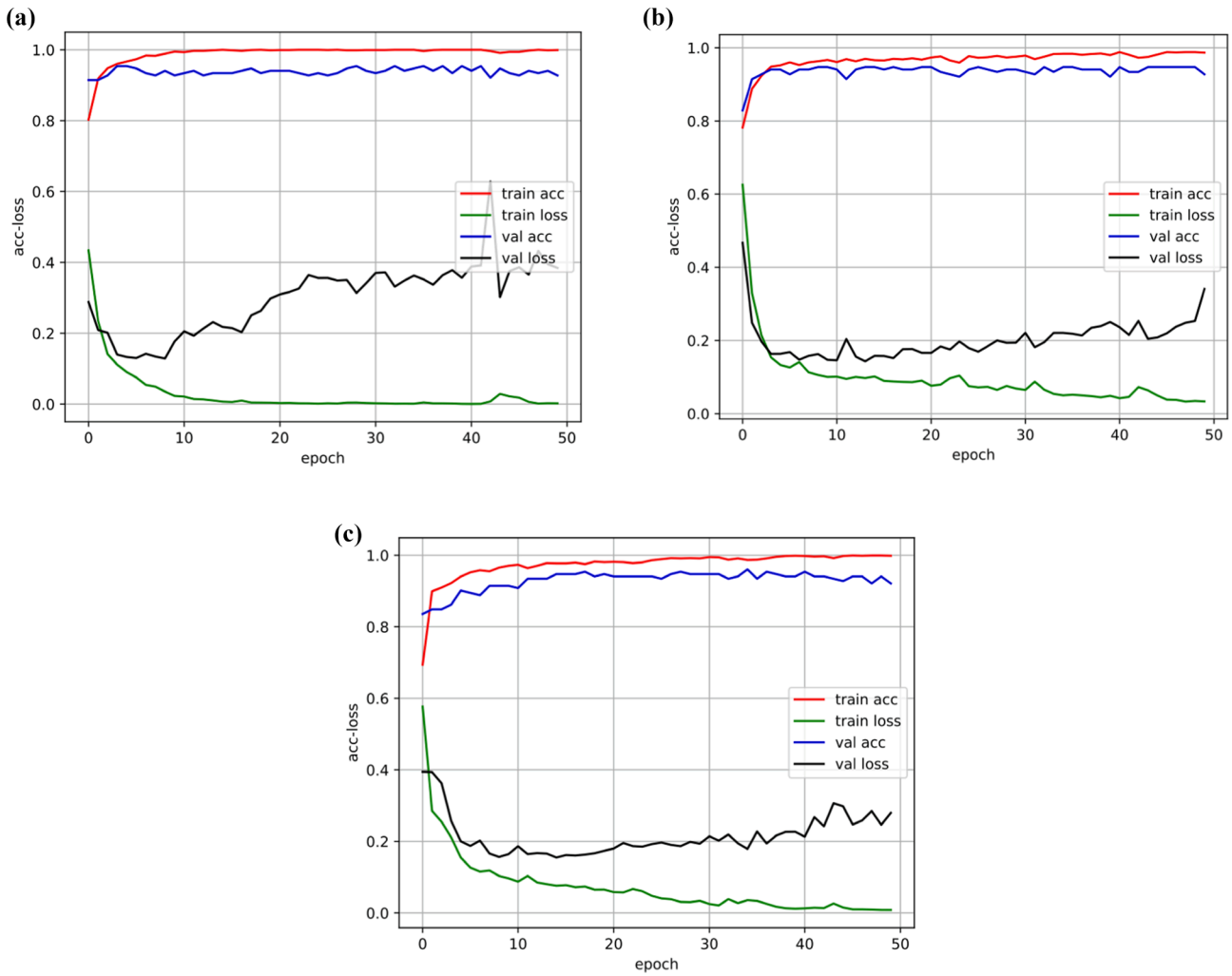

Fig. 4. The accuracy and loss plots of proposed model for the training and validation data using Adam (best optimizer) shows that all the models are well fitted both for the training and validations data in classifying (a) HC vs MCI; (b). MCI vs AD; (c). HC vs AD individuals.

Table 2
Comparison of various CNN models using Adam optimizer.

Model	Performance Index	HC vs MCI	MCI vs AD	HC vs AD
ResNet50	Accuracy	81.7	79.1	87.8
	Sensitivity	81.9	79.3	87.9
	Specificity	81.6	78.9	87.8
VGG16	Accuracy	81.9	83.2	89.3
	Sensitivity	82.3	83.5	89.7
	Specificity	81.4	82.7	88.8
Inception V3	Accuracy	85.3	86.4	89.1
	Sensitivity	85.5	86.7	89.1
	Specificity	84.9	86.1	89
Xception	Accuracy	82.7	81.2	84.8
	Sensitivity	82.9	81.5	84.9
	Specificity	81.8	80.6	84.7
AlexNet	Accuracy	82.8	80.3	87.8
	Sensitivity	82.9	80.5	87.9
	Specificity	82.8	79.8	87.7
Inception-ResNet model	Accuracy	**95.4**	**94.1**	**95.9**
	Sensitivity	**96.5**	**97.3**	**98.4**
	Specificity	**94.1**	**92.1**	**92.2**

Table 3
Comparison of various deep learning models using MRI + PET modalities.

Method	Accuracy (%)	Sensitivity (%)	Specificity (%)	AUC
CNN-RNN [45]	93.26	92.55	93.94	0.957
Bi-LSTM [46]	94.29	96.59	92.38	0.962
FSBi-LSTM [47]	94.82	97.7	92.45	0.968
Proposed Model	**95.06**	97.41	92.76	**0.985**

expensive, complex, and tedious for implementation. However, the study excluded few subjects due to non-availability or artifacts in PET and/or MRI images of the patients and healthy individuals. The current understanding of multi-modal imaging biomarkers for AD are limited for clinical utility.

5. Conclusions

We have developed the Inception-ResNet wrapper CNN model using the fusion of structural MRI and PET imaging features. From this study, we conclude that the proposed Inception-ResNet model outperformed the other existing CNN models with the highest overall average accuracy and ROC in classifying HC, MCI and AD patients. To conclude, the deep learning model with the fusion of MRI-PET imaging modalities improved the accuracy and may be helpful as the automated imaging diagnostic tool for the classification of MCI and AD from HC. In future, the utility of complementary imaging techniques may be useful to improve the clinical diagnosis.

Author Contributions

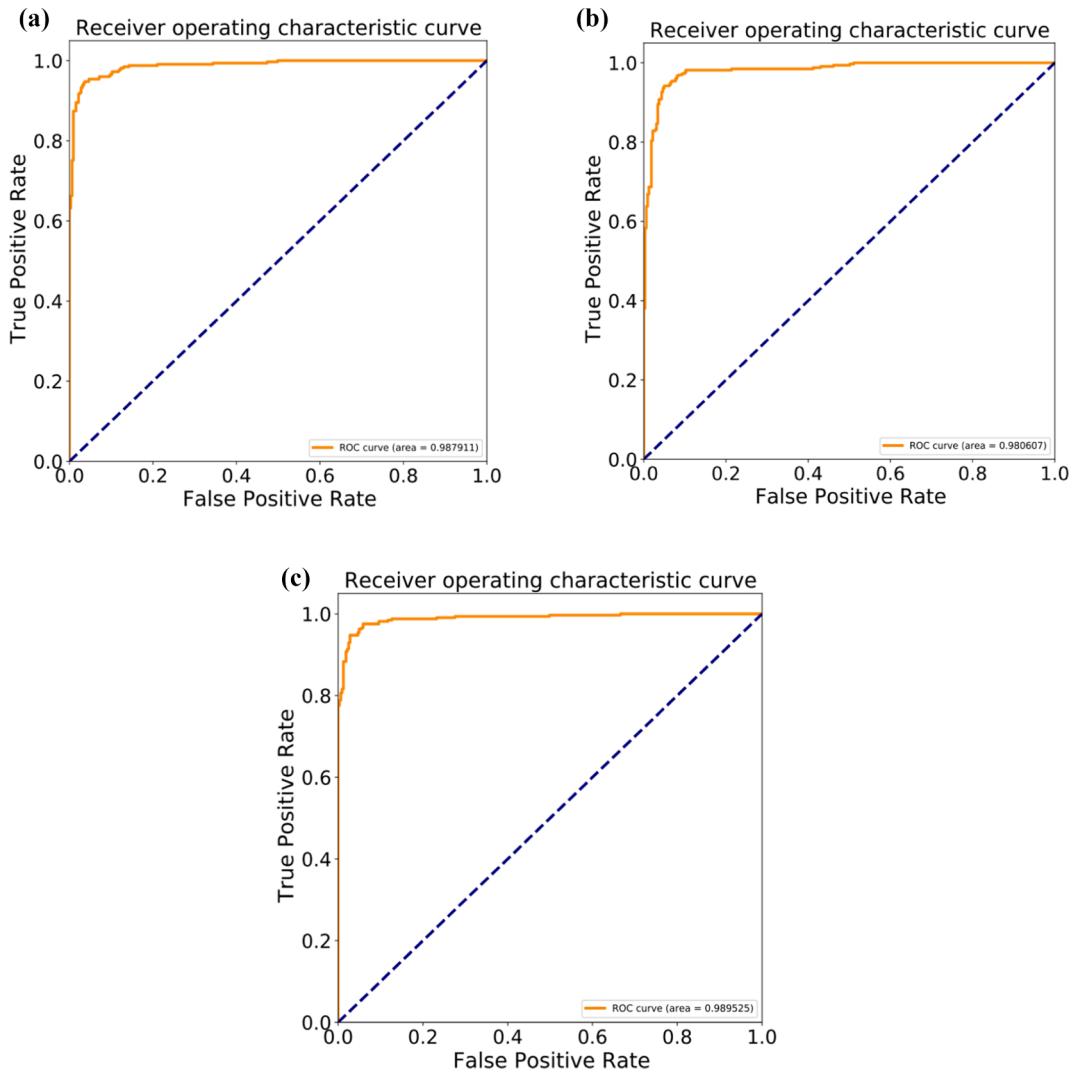

Fig. 5. ROC curves of proposed model using Adam (best optimizer) for classification of (a) HC vs MCI; (b). MCI vs AD; (c). HC vs AD with AUC of 0.988, 0.981 and 0.989 respectively.

VPSR implemented the algorithms and performed data analysis. VPSR and KS design the study and wrote the manuscript.

Declaration of Competing Interest

The authors declare that they have no known competing financial interests or personal relationships that could have appeared to influence the work reported in this paper.

Data availability

The authors do not have permission to share data.

Acknowledgments

Data were provided by OASIS-3: Principal Investigators: T. Benzinger, D. Marcus, J. Morris; NIH P50 AG00561, P30 NS09857781, P01 AG026276, P01 AG003991, R01 AG043434, UL1 TR000448, R01 EB009352. AV-45 doses were provided by Avid Radiopharmaceuticals, a wholly owned subsidiary of Eli Lilly. Also, we would like to acknowledge the anonymous reviewers for their valuable suggestions and comments for improving the manuscript.

References:

[1] J. Prakash, V. Wang, R.E. Quinn III, C.S. Mitchell, Unsupervised machine learning to identify separable clinical Alzheimer's disease sub-populations, Brain Sci. 11 (8) (2021) 977.
[2] C.-H. Chang, C.-H. Lin, H.-Y. Lane, Machine learning and novel biomarkers for the diagnosis of Alzheimer's disease, Int J Mol Sci 22 (5) (2021) 2761.
[3] J.M. Mateos-Pérez, M. Dadar, M. Lacalle-Aurioles, et al., Structural neuroimaging as clinical predictor: a review of machine learning applications, Neuroimage Clin. 20 (2018) 506–522.
[4] W. Liu, L.W.C. Au, J. Abrigo, et al., MRI-based Alzheimer's disease-resemblance atrophy index in the detection of preclinical and prodromal Alzheimer's disease, Aging (Albany NY) 13 (2021) 13496–13514.
[5] O. Keret, A.M. Staffaroni, J.M. Ringman, et al., Pattern and degree of individual brain atrophy predicts dementia onset in dominantly inherited Alzheimer's disease, Alzheimers Dement (Amst) 13 (2021) e12197.
[6] N.J. Herzog, G.D. Magoulas, Brain asymmetry detection and machine learning classification for diagnosis of early dementia, Sensors (Basel) 21 (3) (2021) 778.
[7] B. Li, I. Jang, J. Riphagen, et al., Identifying individuals with Alzheimer's disease-like brains based on structural imaging in the human connectome project aging cohort, Hum Brain Mapp. 42 (2021) 5535–5546.
[8] F. Powell, D. Tosun, A., Raj, for the Alzheimer's Disease Neuroimaging Initiative, Network-constrained technique to characterize pathology progression rate in Alzheimer's disease, Brain Commun. 3: 3 (2021) fcab144.
[9] L. Mosconi, W.H. Tsui, S. De Santi, J. Li, H. Rusinek, A. Convit, Y. Li, M. Boppana, M.J. de Leon, Reduced hippocampal metabolism in MCI and AD: automated FDG-PET image analysis, Neurology. 64 (2005) 1860–1867.
[10] L. Mosconi, W.H. Tsui, K. Herholz, A. Pupi, A. Drzezga, G. Lucignani, E.M. Reiman, V. Holthoff, E. Kalbe, S. Sorbi, et al., Multicenter standardized 18F-FDG PET diagnosis of mild cognitive impairment, Alzheimer's disease, and other dementias, J Nucl Med. 49 (2008) 390–398.

[11] V. Camus, P. Payoux, L. Barre, B. Desgranges, T. Voisin, C. Tauber, R. La Joie, M. Tafani, C. Hommet, G. Chetelat, et al., Using PET with 18F-AV-45 (florbetapir) to quantify brain amyloid load in a clinical environment, Eur J Nucl Med Mol Imaging. 39 (2012) 621–631.
[12] K.R. Gray, R. Wolz, R.A. Heckemann, P. Aljabar, A. Hammers, D. Rueckert, Multi-region analysis of longitudinal FDG-PET for the classification of Alzheimer's disease, Neuroimage. 60 (2012) 221–229.
[13] P.J. Toussaint, V. Perlbarg, P. Bellec, S. Desarnaud, L. Lacomblez, J. Doyon, M. O. Habert, H. Benali, Resting state FDG-PET functional connectivity as an early biomarker of Alzheimer's disease using conjoint univariate and independent component analyses, Neuroimage. 63 (2012) 936–946.
[14] R. Li, R. Perneczky, I. Yakushev, et al., Gaussian mixture models and model selection for [18F] fluorodeoxyglucose positron emission tomography classification in Alzheimer's disease, PLoS One 10 (4) (2015) e0122731.
[15] J. Koivunen, N. Scheinin, J.R. Virta, S. Aalto, T. Vahlberg, K. Nagren, S. Helin, R. Parkkola, M. Viitanen, J.O. Rinne, Amyloid PET imaging in patients with mild cognitive impairment: a 2-year follow-up study, Neurology. 76 (2011) 1085–1090.
[16] A. Okello, J. Koivunen, P. Edison, H.A. Archer, F.E. Turkheimer, K. Nagren, R. Bullock, Z. Walker, A. Kennedy, N.C. Fox, et al., Conversion of amyloid positive and negative MCI to AD over 3 years: an 11C-PIB PET study, Neurology. 73 (2009) 754–760.
[17] M. Pagani, F. De Carli, S. Morbelli, J. Oberg, A. Chincarini, G.B. Frisoni, S. Galluzzi, R. Perneczky, A. Drzezga, B.N. van Berckel et al. Volume of interest-based [18F] fluorodeoxyglucose PET discriminates MCI converting to Alzheimer's disease from healthy controls. A European Alzheimer's Disease Consortium (EADC) study. Neuroimage Clin. 7 (2015) 34–42.
[18] C. Cabral, P.M. Morgado, D. Campos Costa, M. Silveira, Predicting conversion from MCI to AD with FDG-PET brain images at different prodromal stages, Comput Biol Med. 58 (2015) 101–109.
[19] S.F. Eskildsen, P. Coupe, D. Garcia-Lorenzo, V. Fonov, J.C. Pruessner, D.L. Collins, Prediction of Alzheimer's disease in subjects with mild cognitive impairment from the ADNI cohort using patterns of cortical thinning, Neuroimage. 65 (2013) 511–521.
[20] R. Vandenberghe, N. Nelissen, E. Salmon, A. Ivanoiu, S. Hasselbalch, A. Andersen, A. Korner, L. Minthon, D.J. Brooks, K. Van Laere, et al., Binary classification of (18) F-flutemetamol PET using machine learning: comparison with visual reads and structural MRI, Neuroimage. 64 (2013) 517–525.
[21] P. Padilla, M. Lopez, J.M. Gorriz, J. Ramirez, D. Salas-Gonzalez, I. Alvarez, NMF-SVM based CAD tool applied to functional brain images for the diagnosis of Alzheimer's disease, IEEE Trans Med Imaging. 31 (2012) 207–216.
[22] K.R. Gray, P. Aljabar, R.A. Heckemann, A. Hammers, D. Rueckert, Random forest-based similarity measures for multi-modal classification of Alzheimer's disease, Neuroimage. 65 (2013) 167–175.
[23] Y. Fan, S.M. Resnick, X. Wu, C. Davatzikos, Structural and functional biomarkers of prodromal Alzheimer's disease: a high-dimensional pattern classification study, Neuroimage. 41 (2008) 277–285.
[24] C. Davatzikos, P. Bhatt, L.M. Shaw, K.N. Batmanghelich, J.Q. Trojanowski, Prediction of MCI to AD conversion, via MRI, CSF biomarkers, and pattern classification, Neurobiol Aging. 32 (2011) e2319–e2327.
[25] J. Dukart, K. Mueller, H. Barthel, A. Villringer, O. Sabri, M.L. Schroeter, Meta-analysis based SVM classification enables accurate detection of Alzheimer's disease across different clinical centers using FDG-PET and MRI, Psychiatry Res. 212 (2013) 230–236.
[26] X. Zhu, H.I. Suk, D. Shen, A novel matrix-similarity based loss function for joint regression and classification in AD diagnosis, Neuroimage. 100 (2014) 91–105.
[27] W. Zheng, Z. Yao, B. Hu, X. Gao, H. Cai, P. Moore, Novel cortical thickness pattern for accurate detection of Alzheimer's disease, J Alzheimers Dis. 48 (2015) 995–1008.
[28] L.G. Apostolova, K.S. Hwang, O. Kohannim, D. Avila, D. Elashoff, C.R. Jack Jr, L. Shaw, J.Q. Trojanowski, M.W. Weiner, P.M. Thompson, ApoE4 effects on automated diagnostic classifiers for mild cognitive impairment and Alzheimer's disease, Neuroimage Clin. 4 (2014) 461–472.
[29] X. Da, J.B. Toledo, J. Zee, D.A. Wolk, S.X. Xie, Y. Ou, A. Shacklett, P. Parmpi, et al., Integration and relative value of biomarkers for prediction of MCI to AD progression: spatial patterns of brain atrophy, cognitive scores, APOE genotype and CSF biomarkers, Neuroimage Clin. 4 (2014) 164–173.
[30] O. Kohannim, X. Hua, D.P. Hibar, S. Lee, Y.Y. Chou, A.W. Toga, C.R. Jack Jr, M. W. Weiner, P.M. Thompson, Boosting power for clinical trials using classifiers based on multiple biomarkers, Neurobiol Aging. 31 (2010) 1429–1442.
[31] Y. Cui, B. Liu, S. Luo, X. Zhen, M. Fan, T. Liu, W. Zhu, M. Park, T. Jiang, J.S. Jin, Identification of conversion from mild cognitive impairment to Alzheimer's disease using multivariate predictors, PLoS One. 6 (2011) e21896.
[32] C. Hinrichs, V. Singh, G. Xu, S.C. Johnson, Predictive markers for AD in a multi-modality framework: an analysis of MCI progression in the ADNI population, Neuroimage. 55 (2011) 574–589.
[33] F. Liu, L. Zhou, C. Shen, J. Yin, Multiple kernel learning in the primal for multimodal Alzheimer's disease classification, IEEE J Biomed Health Inform. 18 (2014) 984–990.
[34] Z. Dai, C. Yan, Z. Wang, J. Wang, M. Xia, K. Li, Y. He, Discriminative analysis of early Alzheimer's disease using multi-modal imaging and multi-level characterization with multi-classifier (M3), Neuroimage. 59 (2012) 2187–2195.
[35] M. Dyrba, M. Grothe, T. Kirste, S.J. Teipel, Multimodal analysis of functional and structural disconnection in Alzheimer's disease using multiple kernel SVM, Hum Brain Mapp. 36 (2015) 2118–2131.
[36] D. Zhang, D. Shen, Multi-modal multi-task learning for joint prediction of multiple regression and classification variables in Alzheimer's disease, Neuroimage. 59 (2012) 895–907.
[37] G. Yu, Y. Liu, D. Shen, Graph-guided joint prediction of class label and clinical scores for the Alzheimer's disease, Brain Struct Funct. 221 (2016) 3787–3801.
[38] B. Cheng, M. Liu, H.I. Suk, D. Shen, D. Zhang, Multimodal manifold-regularized transfer learning for MCI conversion prediction, Brain Imaging Behav. 9 (2015) 913–926.
[39] B. Cheng, M. Liu, D. Zhang, B.C. Munsell, D. Shen, Domain transfer learning for MCI conversion prediction, IEEE Trans Biomed Eng. 62 (2015) 1805–1817.
[40] M. Amini, M.M. Pedram, A. Moradi, et al., Single and combined neuroimaging techniques for Alzheimer's disease detection, Comput Intell Neurosci. 9523039 (2021).
[41] J. Ramirez, J.M. GoÃrriz, S. Teipel, Editorial: Multimodal and longitudinal bioimaging methods for characterizing the progressive course of dementia, Front Aging Neurosci. 11 (2019) 45.
[42] S. Grueso, R. Viejo-Sobera, Machine learning methods for predicting progression from mild cognitive impairment to Alzheimer's disease dementia: A systematic review, Alzheimers Res Ther. 13 (2021) 162.
[43] Z. Wang, X. Zhu, E.Y. Adeli, et al., Multi-modal classification of neurodegenerative disease by progressive graph-based transductive learning, Med Image Anal. 39 (2017) 218–230.
[44] J. Sheng, M. Shao, Q.R. Zhang, et al., Alzheimer's disease, mild cognitive impairment, and normal aging distinguished by multi-modal parcellation and machine learning, Sci Rep. 10 (2020) 5475.
[45] M. Liu, D. Cheng, W. Yan, The Alzheimer's Disease Neuroimaging Initiative, Classification of Alzheimer's disease by combination of convolutional and recurrent neural networks using FDG-PET images'', Front Neuroinform 12 (35) (2018) 2.
[46] C. Feng, A. Elazab, P. Yang, T. Wang, B. Lei, and X. Xiao. 3D convolutional neural network and stacked bidirectional recurrent neural network for Alzheimer's disease diagnosis. In Proc. 1st Int. Workshop Predictive Intell. Med., (2018) 138-146.
[47] C. Feng, A. Elazab, et al., Deep learning framework for Alzheimer's disease diagnosis via 3D-CNN and FSBi-LSTM, IEEE Access (2019), https://doi.org/10.1109/ACCESS.2019.2913847.
[48] E. Lin, C.-H. Lin, H.-Y. Lane, Deep Learning with neuroimaging and genomics in Alzheimer's disease, Int J Mol Sci. 22 (15) (2021) 7911.
[49] S. Qiu, P.S. Joshi, M.I. Miller, et al., Development and validation of an interpretable deep learning framework for Alzheimer's disease classification, Brain. 143 (2020) 1920–1933, https://doi.org/10.1093/brain/awaa137.
[50] C. Promteangtrong, C. Buchpiguel, Multimodality imaging approach in Alzheimer disease. Part I: Structural MRI, functional MRI, diffusion tensor imaging and magnetization transfer imaging, Dement. Neuropsychol. 9 (2015), https://doi.org/10.1590/1980-57642015DN94000318.9.
[51] P. Lee, H.R. Kim, Y. Jeong, et al., Detection of gray matter microstructural changes in Alzheimer's disease continuum using fiber orientation, BMC Neurol 20 (2020) 362, https://doi.org/10.1186/s12883-020-01939-2.
[53] R.C. Gonzalez, R.E. Woods, Digital Image Processing, Fourth Edition, Pearson Education, 2018.
[54] V.P.S. Rallabandi, P.K. Roy, Magnetic resonance image enhancement using stochastic resonance in Fourier domain, Magnetic Resonance Imaging 28 (9) (2010) 1361–1373.
[55] S.G. Mallat, A theory for multiresolution signal decomposition: The wavelet representation, IEEE Trans Pattern Analysis and Machine Intelligence 11 (1989) 674–693.
[56] G.R. Lee, R. Gommers, F. Wasilewski, K. Wohifahrt, A. O'Leary, PyWavelts: A Python package for wavelet analysis, Journal of Open Source Software. 4 (36) (2019) 1237.
[57] B.B. Avants, N.J. Tustison, M. Stauffer, G. Song, B. Wu, J.C. Gee, The insight toolkit image registration framework, Front Neuroinformatics 8 (2014) 44.
[58] S. Bricq, H.L. Kidane, J. Zavala-Bojorquez, et al., Automatic deformable PET/MRI registration for preclinical studies based on B-splines and non-linear intensity transformation, Med Biol Eng Comput 56 (2018) 1531–1539, https://doi.org/10.1007/s11517-018-1797-0.
[59] S. Gupta, K.P. Ramesh, E.P. Blasch, Mutual information metric evaluation for PET/MRI image fusion, IEEE National Aerospace and Electronics Conference (2008) 305–311, https://doi.org/10.1109/naecon.2008.4806563.
[60] K. Simonyan, A. Zisserman, Very deep convolutional neural networks for large-scale image recognition. In Proc. Computer Vision and Pattern Recognition, CVPR (2014). https://arxiv.org/abs/1409.1556.
[61] G. Huang, et al. Densely connected convolutional networks. In Proc. Computer Vision and Pattern Recognition, CVPR (2016). https://arxiv.org/abs/1608.06993.
[62] A. Krizhevsky, I. Sutskever, G. E. Hinton, ImageNet classification with deep convolutional neural networks. Advances in Neural Information Processing Systems Ed. Pereira F et al., 25 (2012). http://proceedings.neurips.cc/paper/2012/file/c399862d3b9d6b76c8436e924a68c45b-Paper.pdf.
[63] K. He, X. Zhang, S. Ren, J. Sun, Deep residual learning for image recognition. In Proc. Computer Vision and Pattern Recognition, CVPR (2015). https://arxiv.org/abs/1512.0338567.
[64] F. Chollet, Xception: Deep learning with depth-wise separable convolutions. In Proc. Computer Vision and Pattern Recognition, CVPR (2016) https://arxiv.org/abs/1610.02357.
[65] C. Szegedy, et al. Rethinking the inception architecture for computer vision. In Proc. Computer Vision and Pattern Recognition, CVPR (2016). https://arxiv.org/abs/1512.00567.

[66] S. Basheera, M.S. Sai Ram, Convolution neural network-based Alzheimer's disease classification using hybrid enhanced independent component analysis based segmented gray matter of T2-weighted magnetic resonance imaging with clinical valuation, Alzheimers Dement (NY) 5 (2019) 974–986.
[67] S. Basaia, F. Agosta, L. Wagner, et al., Automated classification of Alzheimer's disease and mild cognitive impairment using a single MRI and deep neural networks, Neuroimage Clin 21 (2019), 101645.
[68] J.H. So, N. Madusanka, H.K. Choi, et al., Deep learning for Alzheimer's disease classification using texture features, Curr Med Imaging Rev 15 (2019) 689–698.
[69] J. Kim, B. Lee, Identification of Alzheimer's disease and mild cognitive impairment using multimodal sparse hierarchical extreme learning machine, Hum Brain Mapp 39 (2018) 3728–3741.
[70] D. Lu, K. Popuri, G.W. Ding, et al., Multimodal and multiscale deep neural networks for the early diagnosis of Alzheimer's disease using structural MR and FDG-PET images, Sci Rep 8 (2018) 5697.
[71] H.I. Suk, S.W. Lee, D. Shen, for Alzheimer's Disease Neuroimaging Initiative, Hierarchical feature representation and multimodal fusion with deep learning for AD/MCI diagnosis, Neuroimage 10 (2014) 569–582.
[72] T. Zhou, K.H. Thung, X. Zhu, D. Shen, Effective feature learning and fusion of multimodality data using stage-wise deep neural network for dementia diagnosis, Hum Brain Mapp 40 (2019) 1001–1016.
[73] C. Ieracitano, N. Mammone, A. Hussain, F.C. Morabito, A novel multi-modal machine learning based approach for automatic classification of EEG recordings in dementia, Neural Netw 123 (2020) 176–190.
[74] T.E. Kam, H. Zhang, D. Shen, A novel deep learning framework on brain functional networks for early MCI diagnosis, Med Image Comput Comput Assist Interv. 11072 (2018) 293–301.
[75] T.E. Kam, H. Zhang, Z. Jiao, D. Shen, Deep learning of static and dynamic brain functional networks for early MCI detection, IEEE Trans Med Imaging 39 (2020) 478–487.
[76] M. Wang, C. Lian, et al., Spatial-temporal dependency modeling and network hub detection for functional MRI analysis via convolutional-recurrent network, IEEE Trans Biomed Eng 67 (2019) 2241–2252.
[77] D. Yang, R. Huang, et al., Detection of mild cognitive impairment using convolutional neural network: Temporal-feature maps of functional near-infrared spectroscopy, Front Aging Neurosci 12 (2020) 141.
[78] V.P.S. Rallabandi, K. Seetharaman, The Alzheimer's Disease Neuroimaging Initiative. Classification of cognitively normal controls, mild cognitive impairment and Alzheimer's disease using transfer learning approach, Biomedical Signal Processing and Control 79 (2023), 104092.
[79] V.P.S. Rallabandi, K. Seetharaman, Machine learning-based classification of dementia types: MRI study. In Proc. Int. Conference on Artificial Intelligence and Smart Systems ICAIS 2021, (2021) 109-114.
[80] Y. Chen, J. Storrs, L. Tan, L.J. Mazlack, et al., Detecting brain structural changes as biomarker from magnetic resonance images using a local feature-based SVM approach, J Neurosci Meth 221 (2014) 22–31.
[81] T. Li, W.1. Li, Y.1.Yang, W.1. Zhang, Classification of brain disease in magnetic resonance images using two-stage local feature fusion. PLoS One. 12 (2017) e0171749.
[82] Z. Yang, I.M. Nasrallah, H. Shou, et al., A deep learning framework identifies dimensional representations of Alzheimer's disease from brain structure, Nat Commun. 12 (2021) 7065.
[83] N. Amoroso, D. Diacono, A. Fanizzi, et al., Deep learning reveals Alzheimer's disease onset in MCI subjects: Results from an international challenge, J Neurosci Methods 302 (2018) 3–9.
[84] M. Liu, F. Li, H. Yan, et al., A multi-modal deep convolutional neural network for automatic hippocampus segmentation and classification in Alzheimer's disease, Neuroimage 208 (2020), 116459.
[85] F. Li, M. Liu, for the Alzheimer's Disease Neuroimaging Initiative, Alzheimer's disease diagnosis based on multiple cluster dense convolutional networks, Comput Med Imaging Graph 70 (2018) 101–110.
[86] W. Lin, T. Tong, Q. Gao, et al., Convolutional neural networks-based MRI image analysis for the Alzheimer's disease prediction from mild cognitive impairment, Front Neurosci 12 (2018) 777.
[87] W. Feng, N.V. Halm-Lutterodt, H. Tang, et al., Automated MRI-based deep learning model for detection of Alzheimer's disease process, Int J Neural Syst 30 (2020) 2050032.
[88] M. Liu, D. Cheng, et al., Multi-modality cascaded convolutional neural networks for Alzheimer's disease diagnosis, Neuroinformatics 16 (2018) 295–308.
[89] R.A. Hazarika, D. Kandar, A.K. Maji, An experimental analysis of different deep learning based models for Alzheimer's disease classification using brain magnetic resonance images, J. King Saud Univ.- Comput Inf. Sci. (2021), https://doi.org/10.1016/j.jksuci.2021.09.003.
[90] A. Khan, S. Dubair, An improved multi-modal based machine learning approach for the prognosis of Alzheimer's disease, J. King Saud Univ.- Comput Inf. Sci. (2020), https://doi.org/10.1016/j.jksuci.2020.04.004.
[91] V.P.S. Rallabandi, K. Tulpule, M. Gattu, Automatic classification of cognitively normal, mild cognitive impairment and Alzheimer's disease using structural MRI analysis Informatics in, Medicine Unlocked 18 (2020) 100305.

Further reading

[52] P.J. LaMontagne, T.L.S. Benzinger, J.C. Morris, et al., OASIS-3: Longitudinal neuroimaging, clinical, and cognitive dataset for normal aging and Alzheimer disease, MedRxiv (2019), https://doi.org/10.1101/2019.12.13.19014902.